Efficient Color Boundary Detection with Color-opponent Mechanisms

Kaifu Yang[1], Shaobing Gao[1], Chaoyi Li[1,2], Yongjie Li[1]
[1]University of Electronic Science and Technology of China, Chengdu, China
[2]Shanghai Institutes for Biological Sciences, Chinese Academy of Sciences, Shanghai, China
{yang_kf, gao_shaobing}@163.com, cyli@sibs.ac.cn, liyj@uestc.edu.cn

Abstract

Color information plays an important role in better understanding of natural scenes by at least facilitating discriminating boundaries of objects or areas. In this study, we propose a new framework for boundary detection in complex natural scenes based on the color-opponent mechanisms of the visual system. The red-green and blue-yellow color opponent channels in the human visual system are regarded as the building blocks for various color perception tasks such as boundary detection. The proposed framework is a feedforward hierarchical model, which has direct counterpart to the color-opponent mechanisms involved in from the retina to the primary visual cortex (V1). Results show that our simple framework has excellent ability to flexibly capture both the structured chromatic and achromatic boundaries in complex scenes.

1. Introduction

In natural scenes, color information plays an important role in human visual perception such as shape, texture, and object recognition [1]. From the viewpoint of engineering, color information is also absolutely necessary for various image processing tasks, such as edge detection [2, 3], image segmentation [4], junction/corner detection [2, 5], etc., which are normally basic pre-processing steps for many computer vision applications (e.g., shape-based object recognition). Figure 1 shows a typical example illustrating that some important contours of objects (e.g. flowers) in color natural images are lost in the gray-scale space, especially for those boundaries between the local regions with different colors but equal luminance.

In order to detect edges from color images, many early studies focused on extending those standard edge detectors, such as Sobel, Laplace, Canny operators [6], etc., to color space. These methods are inherently difficult to discriminate salient object boundaries and texture edges due that they respond to all the edges at the luminance or color changes. In recent decades, many new approaches have been developed for edge detection in complex color scenes. Typically, Martin *et al*. [3] took into account multiple local cues (i.e., color, brightness and texture) and combined these cues with a certain learning technique to detect and localize the boundaries. Other learning-based methods tried to take multiple scales [7], more local features [8] or global information [5, 9] for better results. Ren *et al.* [10] also presented a model to enforce the curvilinear continuity with Conditional Random Fields framework. However, the performances of most learning-based methods are strongly dependent on the selection of training sets, which makes the methods inflexible for an individual image. Furthermore, training a method on dataset normally leads to high computational cost.

Figure 1. Example showing that color boundaries are lost when ignoring color information. Color image and its boundary map (**Top**) provide more object information than gray-level image and its boundary map (**Down**).

In addition, a lot of non-learning based algorithms have also been proposed for boundary detection and segmentation in recent years. For example, Zhu *et al.* [11] proposed a contour grouping method with the topological formulation called *untangling cycles*. Salient contours were also extracted by solving the min-cover problem [12] and building Ultrametric Contour Maps [13].

Along another line, the success of biologically based methods for edge detection in gray-level images [14-17] inspired us to build a biologically plausible framework for color boundary detection in natural images in an effect way. Recently, Zhang *et al.* [18] proposed a new color descriptor based on color-opponent mechanisms, which obviously improves the performances of several classical object recognition and boundary detection systems. In addition,

1063-6919/13 $26.00 © 2013 IEEE
DOI 10.1109/CVPR.2013.362

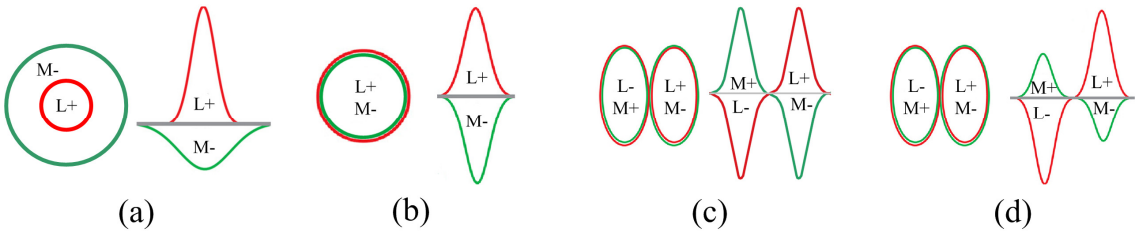

Figure 2. The receptive field of single-opponent cells of Type I (a) and Type II (b) in LGN (lateral geniculate nucleus), and oriented double-opponent cells in V1 with balanced cone-input weightings (c) and unbalanced cone-input weightings (d). Adapted from [19, 20]

several methods based on the two color-opponent channels, i.e., Red-Green (R-G) and Blue-Yellow (B-Y) channels found in human visual system [21], exhibit exciting performance on color boundary detection. In particular, Martin *et al*. [3] computed the color gradients in these two opponent channels for color boundary detection. Zhou and Mel [22] applied custom "pairwise difference" oriented edge detector on the smoothed R-G and B-Y opponent channels. However, one of the key limitations of these opponent-based approaches is that they are blind to the luminance-defined boundaries. In order to obtain the complete contours of objects, these methods had to spend extra computational cost to combine more cues to detect luminance boundaries [3].

Color Mechanisms in the Visual System. It is generally accepted that the human visual system outperforms any existing computer vision system, and therefore, it is attractive to build biologically plausible image processing systems for various computer vision tasks. One of the amazing properties in the human visual system is on the color coding, which can be summarized as follows:

- Trichromacy. There are three kinds of cone photoreceptors, namely L, M, and S cone, at the level of retina, which absorb long, middle and short wavelengths in a local spatial space, respectively. This is well known as trichromacy [21].
- Two opponent channels. It has been known that there are two color opponent channels for transmitting color information along the Retina-LGN (Lateral Geniculate Nucleus)-Cortex pathway, i.e. red-green (R-G) and blue-yellow (B-Y) channel [23-25].
- Color opponency. Many researches have reported that color information is processed in the visual pathway in opponent manners. The ganglion or LGN cells are found to have single-opponent receptive field (RF) and cells in the primary visual cortex (V1) have double-opponent RF [19, 26]. There are mainly two types of single-opponent cells in LGN: Type I cells have center-surround opponent RF (Figure 2(a)) and in contrast, Type II cells have center-only opponent RF (Figure 2(b) [27, 28]. In V1, the RF of neurons shows more complex properties. Their RFs are both chromatically and spatially opponent [28-30]. Especially, It has been reported that some neurons in V1, called oriented double-opponent neurons, are orientation-selective for both chromatic and achromatic patterns [31], which was considered to play a crucial role in boundary detection in (color) natural scenes. Subsequently, some authors have proposed several computational models to describe the orientation-selective RF of V1 neurons. For example, double-opponent RF was modeled as two single-opponent RFs with opposite sign placed side-by-side [20]. The RF structure with balanced cone-input weightings is shown in Figure 2(c), which can respond well to color-defined boundaries [20]. Subsequently, RF structure with unbalanced cone weightings was also reported (Figure 2(d)) [19, 26], and the cells with such RF structure may respond to both achromatic and iso-luminant gratings.

In this paper, we introduce a new biologically plausible model that exhibits better performance on capturing simultaneously both chromatic and achromatic boundaries. The new model includes three layers (Figure 3). In detail, in the first layer (Cone layer), Gaussian filters simulating cone RFs are used to obtain local information on individual color component (red, green, blue and yellow) of the input color image. In the Ganglion/LGN layer, the responses of single-opponent neurons are computed with two pairs of opponent color components: R-G/G-R and B-Y/Y-B. In the last layer (Cortex layer), multiple oriented double-opponent filters are used to extract boundaries and a max operator is used to combine boundaries over all orientations in each opponent channel. Finally, we compute the maximum to combine the boundaries across all opponent channels.

As briefly mentioned above, in this work, we simulate the biological mechanisms of color information processing along the Retina-LGN-Cortex visual pathway and propose a feedforward hierarchical system for boundary detection in real natural scenes. The results on a commonly used dataset show that our model has the capacity of simultaneously detecting the color- and luminance-defined boundaries. In addition, our model has obvious advantage in saving computational cost.

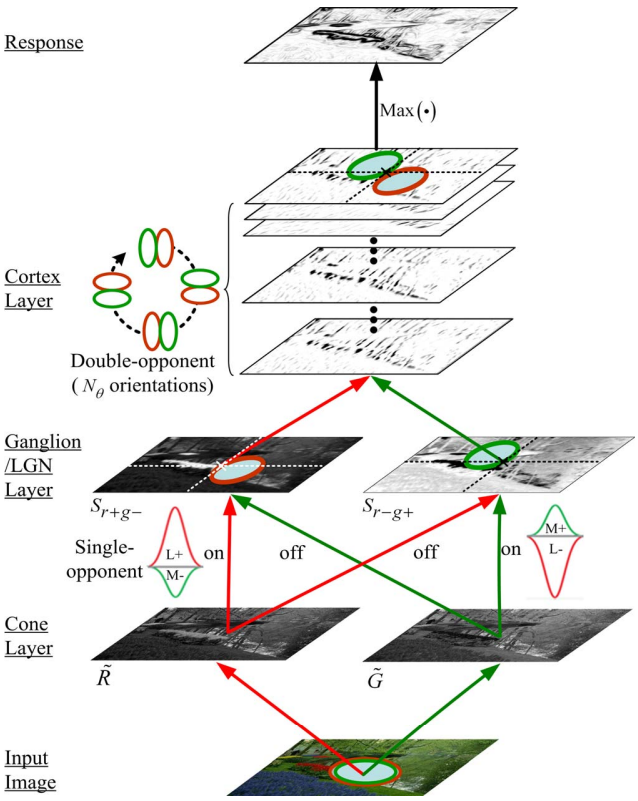

Figure 3. The flowchart of our framework for boundary detection in the R-G channel. The similar computational steps are used in the other channels.

2. Boundary Detection System

Our framework is a feedforward hierarchical model including three layers, which correspond to the level of retina, LGN and primary visual cortex (V1) of the visual system, respectively. We have found previously that the computational role of the single-opponent RF of Type II cells (Figure 2(b)) in the ganglion/LGN layer is mainly for the perception of color region, and in the present study, we focus on the oriented double-opponent neurons (Figure 2(c-d)) in V1 for the specific boundary detection task because of their orientation-selective property for both the of chromatic and achromatic patterns [31].

The general flowchart is summarized in Figure 3, in which we just show the computational steps in the R-G channel, and the other channels share the similar computational steps.

Cone Layer: In the first layer, the input color image is separated into four channels: red (R), green (G), blue (B) and yellow (Y) components, where Y = (R+G)/2. In order to obtain the local color information, Gaussian filters are used to simulate the receptive field of the cones in the retina [19, 20]. The standard deviation of Gaussian controls the size of receptive field. We use Gaussian filters with same standard deviate (σ) for each channel. The cone outputs of the four channel are denoted by $\tilde{R}$, $\tilde{G}$, $\tilde{B}$ and $\tilde{Y}$, respectively.

Ganglion/LGN Layer: Generally, the retinal ganglion cells and LGN cells have similar RF properties. Here we implement the processing of ganglion layer and LGN into a single layer. The cells in the ganglion/LGN layer have single-opponent receptive fields and show spatially low-pass property. The cells in this layer receive the cone outputs, and their responses can be described as

$$S(x,y) = w_1 \bullet \tilde{R}(x,y;\sigma) + w_2 \bullet \tilde{G}(x,y;\sigma) \quad (1)$$

$$\text{where , } \begin{cases} w_1 w_2 \le 0 \\ |w_1|,|w_2| \in [0,1] \end{cases} \quad (2)$$

where w_1 and w_2 are the connection weightings from cones to ganglion cells. w_1 and w_2 always have opposite sign. With $w_1 > 0$ and $w_2 < 0$, we obtain the responses of R-on/G-off cells, and with $w_1 < 0$ and $w_2 > 0$, we get the responses of R-off/G-on cells (Figure 3).

Single-opponent cells in ganglion/LGN layer are important for separating color and achromatic information, which is clearly shown by Equation 1. When the ganglion/LGN cells have balanced cone-input weightings, i.e. $|w_1| = |w_2|$, the ganglion/LGN cells may be blind to achromatic information, because achromatic information provides same component values in different channels and w_1 and w_2 are in opposite sign. In contrast, when the cone-input weightings are unbalanced (i.e. $|w_1| \neq |w_2|$), the model has the ability of detecting luminance changes. Their contributions to the final boundary detection are different, as described in Section 3.

Cortex Layer: In the cortex layer of V1, the receptive fields of most color- and color-luminance-sensitive neurons are both chromatically and spatially opponent. In particular, the oriented double-opponent cells are considered to play an important role in color boundary detection [31]. We simulate the receptive fields of these oriented double-opponent V1 cells shown in Figure 2(c-d) as

$$RF(x,y;\theta) = \left| \frac{\partial f(\tilde{x},\tilde{y})}{\partial \tilde{x}} \right| \quad (3)$$

$$f(\tilde{x},\tilde{y}) = \frac{1}{\sqrt{2\pi(k\sigma)^2}} \exp\left(\frac{-(\tilde{x}^2 + \gamma^2 \tilde{y}^2)}{2(k\sigma)^2}\right) \quad (4)$$

$$\begin{bmatrix} \tilde{x} \\ \tilde{y} \end{bmatrix} = \begin{bmatrix} x\cos\theta + y\sin\theta \\ -x\sin\theta + y\cos\theta \end{bmatrix} \quad (5)$$

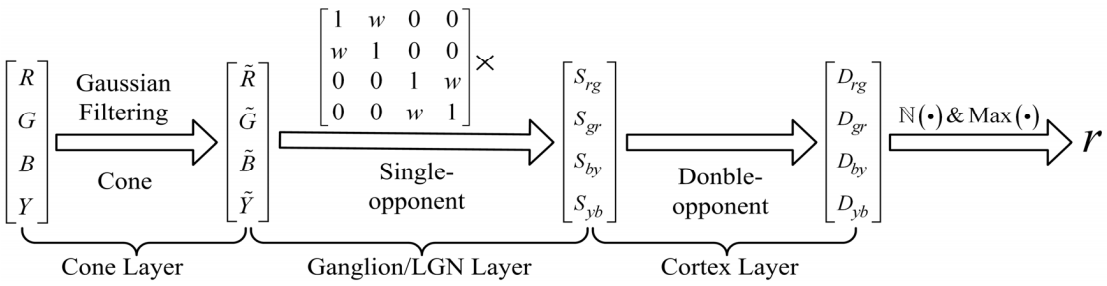

Figure 5. The full computational steps of the proposed system for color boundary detection. $\mathbb{N}(\cdot)$ denotes the linear normalization.

In Equation 4, γ is the spatial aspect ratio of Gaussian that controls the ellipticity of receptive field. In this study we set $\gamma = 0.5$ based on the physiological finding [19, 26]. $\theta \in [0, 2\pi)$ is the preferred orientation of a given cell. We set $k = 2$ and σ to be same as the scale of Gaussian filters used in the ganglion/LGN layer. $k\sigma$ determines the RF size of V1 neurons and $k > 1$ means that V1 neurons have larger RF than that of the ganglion/LGN cells.

Figure 4(left) shows a simple example of RF model of the oriented double-opponent neurons in V1 with vertical orientation. The vertical axis separates the filter into two parts: the left part receives the R-on/G-off response (S_{r+g-}) and the right receives the R-off/G-on response (S_{r-g+}) of ganglion/LGN cells. The vertical axis indicates the orientation of boundary that can be extracted by this filter.

Figure 4(right) shows that the neuron with $\theta = \alpha$ responds to the R-to-G boundary; in contrast, the neuron with $\theta = \alpha + \pi$ can detect the G-to-R boundary. Taken together, we employ a set of filters with orientations $\theta \in [0, 2\pi)$ to detect the boundaries defined by the same color pairs but with different polarities.

The boundary responses at each orientation is given by

$$D(x, y; \theta_i) = \sum_{m,n \in N_{r+g-}} S_{r+g-}(x+m, y+n) \bullet RF(m, n; \theta_i) + \sum_{m,n \in N_{r-g+}} S_{r-g+}(x+m, y+n) \bullet RF(m, n; \theta_i) \quad (6)$$

where $S_{r-g+} = -S_{r+g-}$, N_{r+g-} and N_{r-g+} are the R-on/G-off and R-off/G-on RF regions of V1 neurons, respectively. $\theta_i \in [0, 2\pi)$ are N_θ different orientations computed at

$$\theta_i = \frac{2(i-1)\pi}{N_\theta}, i = 1, 2, \cdots, N_\theta. \quad (7)$$

In this work, we set $N_\theta = 16$.

Then, a max mechanism is used across all orientations to obtain the responses to the boundaries in R-G opponent channel according to

$$D(x, y) = \max\{D(x, y; \theta_i) \mid i = 1, 2, ..., N_\theta\} \quad (8)$$

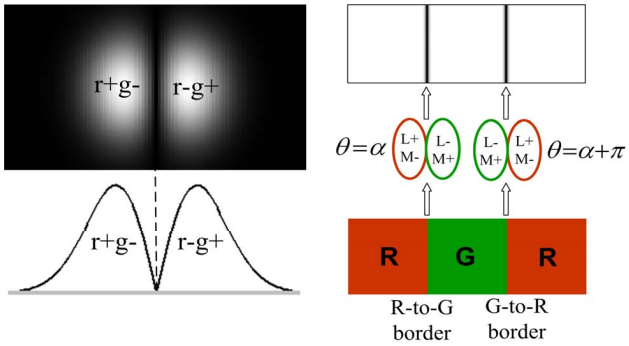

Figure 4. **Left:** The receptive field model of the oriented double-opponent neurons in V1 with vertical orientation. It includes two spatially separated parts, which receive opposite opponent outputs from LGN. **Right:** Two neurons with 180 degree difference between their preferred orientations ($\theta = \alpha$ and $\theta = \alpha + \pi$) detect the color boundaries with the same orientation but different polarities (i.e., R-to-G vs. G-to-R).

The Full Model: For the convenience of computation, we set one of w_1 and w_2 as 1, and another one as $w \in [-1, 0]$ to meet Equation 2. Then the boundaries are detected in four channels (i.e., $\tilde{R} + w\tilde{G}$, $w\tilde{R} + \tilde{G}$, $\tilde{B} + w\tilde{Y}$ and $w\tilde{B} + \tilde{Y}$) with Equations 1-8. The full computational flowchart is summarized in Figure 5.

From Figure 5, the output of each channel is first normalized linearly. The final output is obtained by taking the max response over channels at each location according to

$$r(x, y) = \max(D_{c_i}(x, y) \mid c_i \in \{rg, gr, by, yb\}) \quad (9)$$

We call our system as $CO(w)$, which means the color opponent (CO) system with a cone-input weighting of w.

3. Experiments

To begin with, we evaluate the effect of the cone-input weightings (i.e. w in Figure 5) on the performance of the proposed model. Figure 6 illustrates the different responses of our model $CO(w)$ to color and achromatic boundaries with different w. It is clear that when $w = -1.0$ (i.e.,

$|w_1| = |w_2|$ in Equation 1), our $CO(-1.0)$ method is blind to luminance-defined boundaries. When w varies from -1.0 to 0.0, the responses to luminance-defined boundaries increase. Taken together, when $w \neq -1.0$ (i.e., $|w_1| \neq |w_2|$), our model has the exciting ability of extracting the color- and luminance-defined boundaries simultaneously with an opponent way. For the pure color and brightness boundaries (top row in Figure 6), the model shows equivalent responses to the two types of boundaries when $w = 0$. In contrast, both the color- and luminance-defined boundaries in the natural image (bottom row in Figure 6) are well responded when $w = -0.6$. This may because that the absolute values of color difference are normally weaker than that of the brightness difference in natural images.

We designed synthetic images with broken circles at different noise levels to verify the capacity of our model to extract smooth contours in noised images. Figure 7 clearly shows that our model has wonderful ability of suppressing the noises while reconstructing the broken portions of the contours. With the increasing of the scale σ, the smooth circles can pop-out more clearly from the noised background, which is mainly the contribution of the local Gaussian filter in the Cone layer.

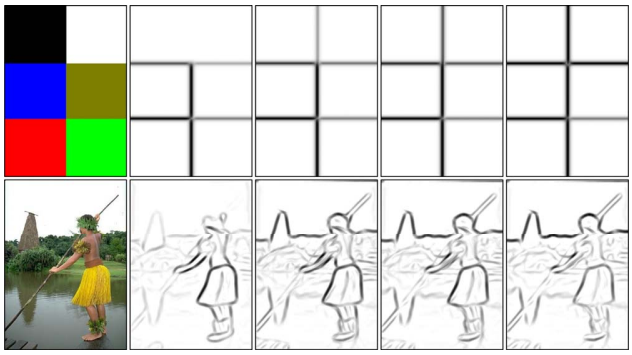

Figure 6. The proposed model responds differently to color and achromatic boundaries with various cone-input weightings. **From left to right:** Original images and the responses of $CO(w)$ with different cone-input weightings (w): -1.0, -0.6, -0.4 and 0.0. Note that the four color blocks in the artificial image of the top row have pure colors, i.e., they are of equi-luminance.

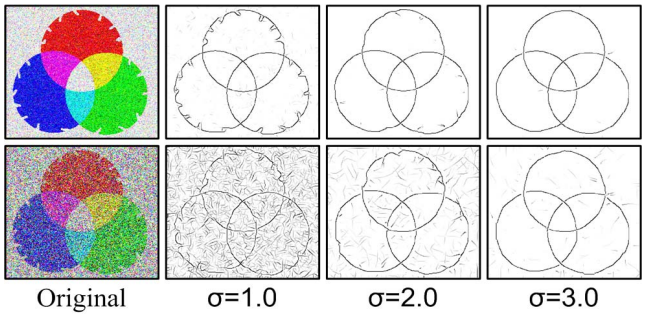

Figure 7.The capacity of our model to reconstruct broken contours while suppressing noise. **From left to right**: synthetic images and the responses of our model at different filter scales (σ) in the Cone layer. The top and bottom rows are the images added with low- and high-level random noises.

We further evaluated the performance of our model using a publicly available dataset, i.e., Berkley Segmentation Data Set (BSDS300), provided by Martin *et al*. [32]. Each image in the dataset has multiple human-marked segmentations. For convenient comparison, the pixel values of the output images (i.e., the boundaries) of all detectors denote the probability of being object boundaries after an operation of non-maxima suppression [14-17]. In order to evaluate the performance quantitatively, we also computed the so-called *F-measure*, defined as $F = 2PR/(R+P)$, following the manners described in [3]. *P* and *R* represent precision and recall, which have been widely used for evaluating the performance of edge detectors [3, 33].

In Figure 8, we compared our model with the *Pb* detector proposed by Martin *et al*. [3]. The boundaries of each image with different w are presented in Figure 8 (the forth to the eighth column), and the optimal results are marked with bold rectangles. It is clear from Figure 8 that our model exhibits more powerful ability of extracting the structured object boundaries with lower color or brightness contrast. Furthermore, our model has the ability to detect the color or achromatic boundaries in a flexible manner. By selecting a suitable value of w , the optimal boundary detection result for individual images can be achieved.

In contrast, the *Pb* method detects brightness, color and texture boundaries separately, and then combines them with a specific supervised learning technique. As a result, the performance is strongly dependent on the training sets, and it is inflexible to obtain the optimal result for individual images. In addition, in order to obtain the color and brightness boundaries of objects, more computational costs are required to detect color and brightness information separately, train and combine multiple cues, such as [3].

The last column in Figure 8 shows the quantitative comparison of our $CO(w)$ model with *Pb*. The maximum F-measure, which was computed from the probability of boundary map at a specific threshold, captures the trade-off between precision and recall [3]. The red dotted horizontal line indicates the optimal performance of *Pb*. It is clear that our $CO(w)$ model provides higher F-measure at most w levels; particularly, the maximum of F-measure over different w (corresponding to the optimal detection results) is notably higher for our model than for *Pb*, at least for the three specific images in Figure 8. Such property of our $CO(w)$ provides us a wide space to introduce new ways to improve our model in the future work by adaptively selecting optimal w for each image, considering another remarkable advantage of $CO(w)$ in saving computational

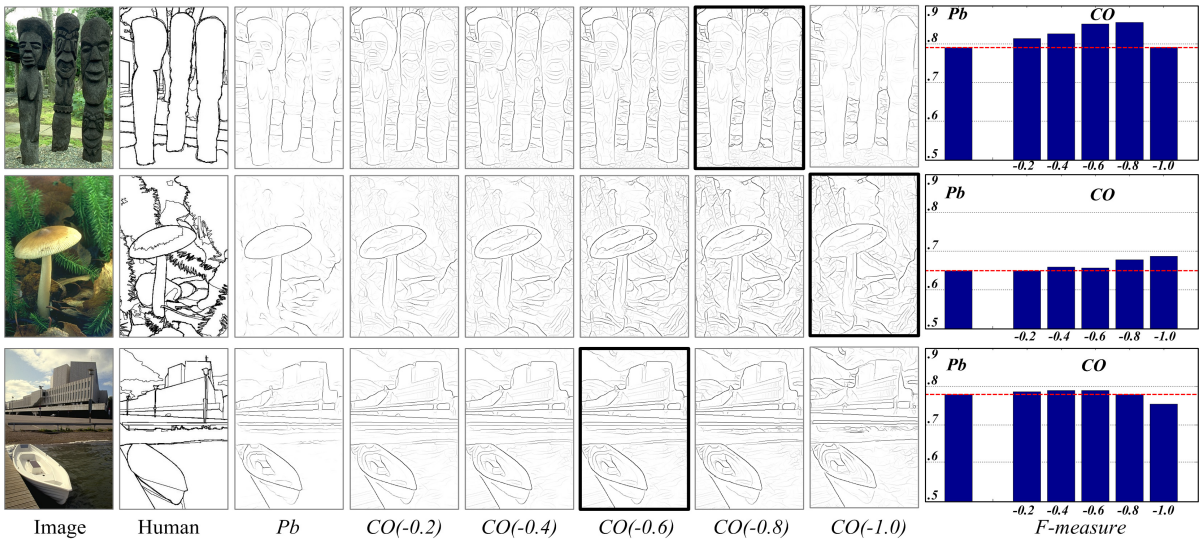

Figure 8. Comparisons of our model $CO(w)$ (with $\sigma = 1.5$ and different cone-input weightings w) with Pb detector [3]. The last column presents the F-measure of each boundary map listed in the third to eighth columns. The optimal results (marked by black bold rectangle) correspond to the maximum of F-measure.

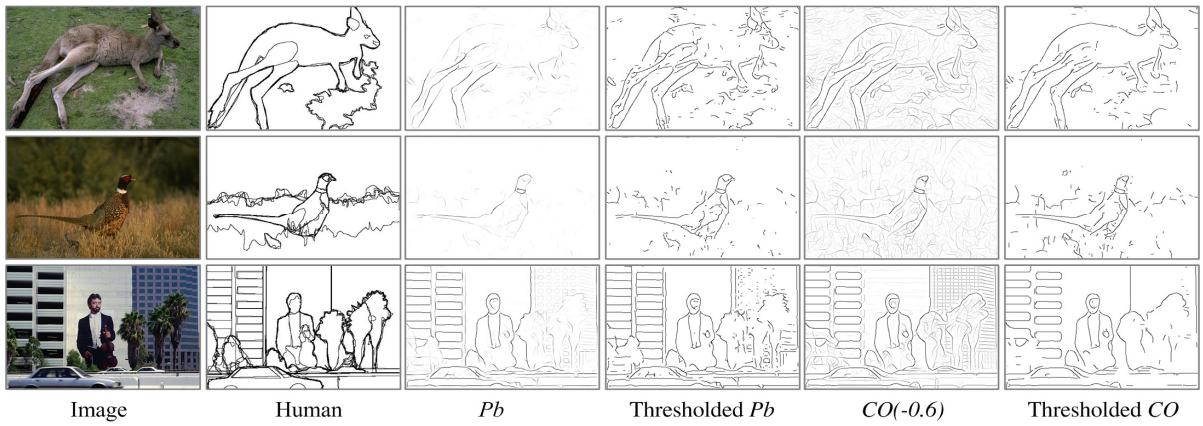

Figure 9. More examples compared with *Pb*. From thresholded *Pb* and thresholded *CO*, our $CO(-0.6)$ removes more cluttered weak edges and reserves more complete boundaries. The thresholds used here correspond to the maximal *F-measure* for each image.

cost (see details later).

Figure 9 presents more examples. Although our method responds to more texture edges, which may be useless for some high-level visual perceptions (such as shape-based object recognition), the responses to texture edges are usually quite weaker than boundaries (the fifth column in Figure 9). Therefore, with a suitable threshold, our detector can easily reduce many cluttered weak edges, as shown in the last column in Figure 9.

Another point worthy of noticing is that our model has higher resolution when extracting the boundaries that are very close to each other. Figure 10 shows several typical examples with zoomed local regions.

We further evaluate the effect of w on the performance of contour detection. From Figure 11, our $CO(w)$ achieves the optimal performance with $w = -0.6$ and $\sigma = 1.5$ (i.e. $CO(-0.6)$). The overall performance of $CO(-0.6)$ is very similar to *Pb* (F = 0.64 for $CO(-0.6)$ vs. F = 0.65 for *Pb*). Furthermore, our $CO(-1.0)$ outperforms *CG*, both of which detect only color boundaries. This implies that our model is superior in utilizing color information.

More comparisons are listed in Table 1. our $CO(-0.6)$ performs as excellent as several novel methods proposed in recent years, e.g., the methods in [3, 10, 11], though several multiscale extensions of *Pb* achieve higher performance [7, 9]. Furthermore, our model has a remarkable advantage in saving computational cost (Table 2): our model just takes about a tenth of the time needed by *Pb* and need no extra training process. Considering the fact that the other models except *Pb* presented in Table 1 are various extended versions of *Pb*, they obviously should take more time (not

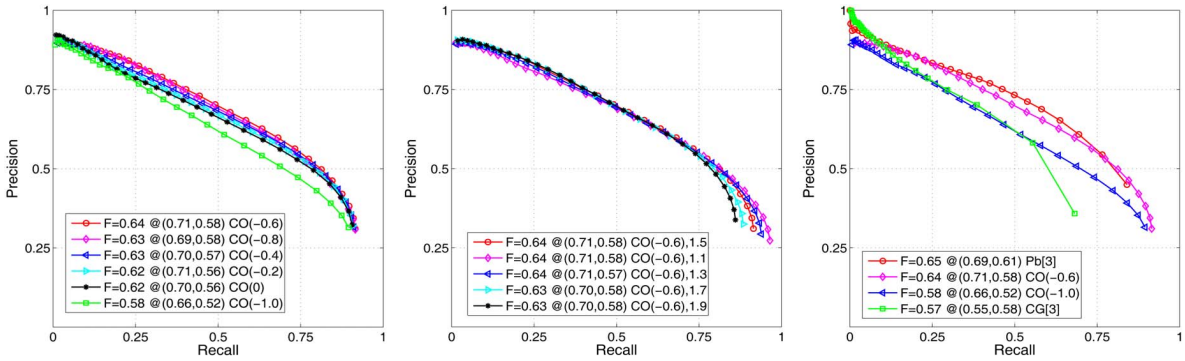

Figure 11. Precision recall curves of $CO(w)$, *Pb*[3] and *CG*[3] on color test images of BSDS300. **Left**: The performances of our methods with different cone-input weightings at a certain scale ($\sigma = 1.5$). **Middle**: The performances of $CO(-0.6)$ with different scales: $\sigma =$ 1.1, 1.3, 1.5, 1.7, and 1.9. $\sigma = 1.5$ is best for our model. **Right**: the overall performance of different methods on the 100 test images of BSDS300 [32].

shown here) than *Pb*. Taken together, we believe that our model is especially useful in some speed-concerned applications requiring real-time processing, such as video processing, etc.

Method	F-measure
Ours (CO(-0.6))	0.64
gPb –Arbelaez, et al. (2011) [9]	0.70
Multiscale – Ren (2008) [7]	0.68
Untangling Cycles –Zhu et al. (2007) [11]	0.64
CRF– Ren et al. (2005) [10]	0.64
Pb– Martin et al. (2004) [3]	0.65

Table 1. Comparing to more color boundary detectors.

Method	*CG* [3]	*Pb* [3]	$CO(w)$
Time (s)	29.64	49.00	5.37

Table 2. Mean computation time taken to compute one boundary map averaged over the 100 test images in BSDS300 [32] with MATLAB codes. Computer used here is Intel Core2, 2.8GHZ with 2.0G RAM.

4. Conclusions and Future Work

This paper presented a novel biologically plausible computational model for contour detection of color images. We try to build an efficient model by simulating the processing manners from the retina to the primary cortex (V1) of the human visual system. Local information is processed hierarchically with the single-opponent cells at the ganglion/LGN levels and the double-opponent cells in V1. Our model exhibits excellent capability of detecting both color and luminance boundaries synchronously in a time-saving manner.

Color-luminance cells (29%) in V1 respond to both the color and achromatic information, but there are also specific neurons in V1 responding exclusively to either color (11%) or luminance (60%) information [31]. How to integrate color and luminance information in V1 or higher level cortexes of the visual system is less known. In addition, combination of various visual cues (color, orientation, luminance, etc.) [34, 35] and the context influence between neurons also arouse widely concern [36, 37]. Our future work will focus on integrating different cues (at multiple scales) processed in V1 into a unified model for contour detection or other computer vision tasks.

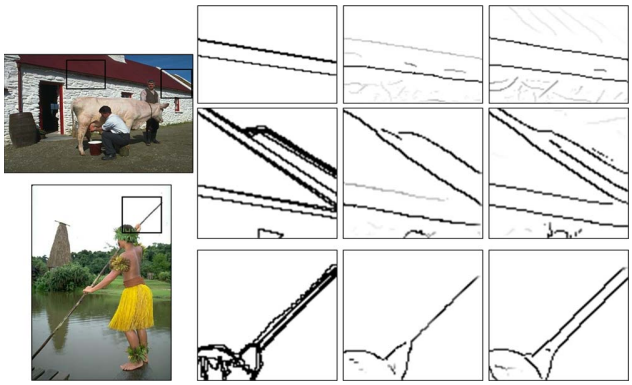

Figure 10. Zoomed in view of two test images. **From left to right:** original images with local regions of interest (black rectangle), human-marked boundaries, boundaries detected by *Pb* and our $CO(-0.6)$.

Acknowledgements

This work was supported by the Major State Basic Research Program (#2013CB329401), the Natural Science Foundations of China (#61075109, #90820301, #91120013) and the Outstanding Doctoral Support Program of University of Electronic Science and Technology of China (#YBXSZC20131041). The work was also partially supported by the 111 Project (#B12027) and PCSIRT (#IRT0910) of China.

References

[1] S. K. Shevell and F. A. A. Kingdom, "Color in Complex Scenes," *Annu. Rev. Psychol.,* vol. 59, pp. 143-166, 2008.

[2] M. A. Ruzon and C. Tomasi, "Edge, junction, and corner detection using color distributions," *IEEE Trans. on PAMI,* vol. 23, pp. 1281-1295, 2001.

[3] D. R. Martin, C. C. Fowlkes, and J. Malik, "Learning to detect natural image boundaries using local brightness, color, and texture cues," *IEEE Trans. on PAMI,* vol. 26, pp. 530-549, 2004.

[4] J. Fan, D. K. Y. Yau, A. K. Elmagarmid, and W. G. Aref, "Automatic image segmentation by integrating color-edge extraction and seeded region growing," *IEEE Trans. on Image Processing,,* vol. 10, pp. 1454-1466, 2001.

[5] M. Maire, P. Arbeláez, C. Fowlkes, and J. Malik, "Using contours to detect and localize junctions in natural images," in *CVPR*, 2008, pp. 1-8.

[6] J. Canny, "A computational approach to edge detection," *IEEE Trans. on PAMI,* pp. 679-698, 1986.

[7] X. Ren, "Multi-scale improves boundary detection in natural images," in *ECCV*, 2008, pp. 533-545.

[8] P. Dollar, Z. Tu, and S. Belongie, "Supervised learning of edges and object boundaries," in *CVPR*, 2006, pp. 1964-1971.

[9] P. Arbelaez, M. Maire, C. Fowlkes, and J. Malik, "Contour detection and hierarchical image segmentation," *IEEE Trans. on PAMI,* vol. 33, pp. 898 - 916, 2011.

[10] X. Ren, C. C. Fowlkes, and J. Malik, "Scale-invariant contour completion using conditional random fields," in *ICCV*, 2005, pp. 1214-1221.

[11] Q. Zhu, G. Song, and J. Shi, "Untangling cycles for contour grouping," in *ICCV*, 2007, pp. 1-8.

[12] P. Felzenszwalb and D. McAllester, "A min-cover approach for finding salient curves," in *POCV*, 2006, pp. 185-185.

[13] P. Arbelaez, "Boundary extraction in natural images using ultrametric contour maps," in *POCV*, 2006, pp. 182-182.

[14] C. Zeng, Y. Li, and C. Li, "Center-Surround Interaction with Adaptive Inhibition: A Computational Model for Contour Detection," *Neuroimage,* vol. 55, pp. 49-66, 2011.

[15] G. Papari, P. Campisi, N. Petkov, and A. Neri, "A biologically motivated multiresolution approach to contour detection," *EURASIP Journal on Applied Signal Processing,* vol. 2007, pp. 119-119, 2007.

[16] N. Petkov and M. A. Westenberg, "Suppression of contour perception by band-limited noise and its relation to nonclassical receptive field inhibition," *Biological Cybernetics,* vol. 88, pp. 236-246, 2003.

[17] C. Grigorescu, N. Petkov, and M. A. Westenberg, "Contour detection based on nonclassical receptive field inhibition," *IEEE Trans. on Image Processing,* vol. 12, pp. 729-739, 2003.

[18] J. Zhang, Y. Barhomi, and T. Serre, "A New Biologically Inspired Color Image Descriptor," in *ECCV*, 2012, pp.312-324

[19] B. R. Conway*, et al.*, "Advances in color science: from retina to behavior," *The Journal of Neuroscience,* vol. 30, pp. 14955-14963, 2010.

[20] S. G. Solomon and P. Lennie, "The machinery of colour vision," *Nature Reviews Neuroscience,* vol. 8, pp. 276-286, 2007.

[21] P. K. Kaiser, R. M. Boynton, and W. H. Swanson, *Human color vision*. Vol. 287. Washington DC: Optical Society of America, 1996.

[22] C. Zhou and B. W. Mel, "Cue combination and color edge detection in natural scenes," *Journal of Vision,* vol. 8, pp. 1-25, 2008.

[23] K. R. Gegenfurtner, "Cortical mechanisms of colour vision," *Nature Reviews Neuroscience,* vol. 4, pp. 563-572, 2003.

[24] R. L. De Valois, I. Abramov, and G. H. Jacobs, "Analysis of response patterns of LGN cells," *JOSA,* vol. 56, pp. 966-977, 1966.

[25] A. M. Derrington, J. Krauskopf, and P. Lennie, "Chromatic mechanisms in lateral geniculate nucleus of macaque," *The Journal of Physiology,* vol. 357, pp. 241-265, 1984.

[26] R. Shapley and M. Hawken, "Color in the cortex--Single-and double-opponent cells," *Vision Research,* vol. 51, pp. 701-717, 2011.

[27] T. N. Wiesel and D. H. Hubel, "Spatial and chromatic interactions in the lateral geniculate body of the rhesus monkey," *Journal of Neurophysiology,* vol. 29, pp. 1115-1156 1966.

[28] B. R. Conway, "Spatial structure of cone inputs to color cells in alert macaque primary visual cortex (V-1)," *The Journal of Neuroscience,* vol. 21, pp. 2768-2783, 2001.

[29] E. N. Johnson, M. J. Hawken, and R. Shapley, "The orientation selectivity of color-responsive neurons in macaque V1," *The Journal of Neuroscience,* vol. 28, pp. 8096-8106, 2008.

[30] R. Shapley and M. Hawken, "Neural mechanisms for color perception in the primary visual cortex," *Current Opinion in Neurobiology,* vol. 12, pp. 426-432, 2002.

[31] E. N. Johnson, M. J. Hawken, and R. Shapley, "The spatial transformation of color in the primary visual cortex of the macaque monkey," *Nature Neuroscience,* vol. 4, pp. 409-416, 2001.

[32] D. Martin, C. Fowlkes, D. Tal, and J. Malik, "A database of human segmented natural images and its application to evaluating segmentation algorithms and measuring ecological statistics," in *ICCV*, 2001, pp. 416 - 425.

[33] I. E. Abdou and W. K. Pratt, "Quantitative design and evaluation of enhancement/thresholding edge detectors," *Proceedings of the IEEE,* vol. 67, pp. 753-763, 1979.

[34] Z. M. Shen, W. F. Xu, and C. Y. Li, "Cue invariant detection of centre–surround discontinuity by V1 neurons in awake macaque monkey," *The Journal of Physiology,* vol. 583, pp. 581-592, 2007.

[35] J. Rivest and P. Cabanagh, "Localizing contours defined by more than one attribute," *Vision Research,* vol. 36, pp. 53-66, 1996.

[36] G. Loffler, "Perception of contours and shapes: Low and intermediate stage mechanisms," *Vision Research,* vol. 48, pp. 2106-2127, 2008.

[37] P. Seriès, J. Lorenceau, and Y. Frégnac, "The "silent" surround of V1 receptive fields: theory and experiments," *Journal of physiology-Paris,* vol. 97, pp. 453-474, 2003.